Growth of $BaSi_2$ continuous films on Ge(111) by molecular beam epitaxy and fabrication of p-$BaSi_2$/n-Ge heterojunction solar cells

Ryota Takabe, Suguru Yachi, Daichi Tsukahara, Kaoru Toko, and Takashi Suemasu*
Institute of Applied Physics, University of Tsukuba, Tsukuba, Ibaraki 305-8573, Japan
*E-mail: suemasu@bk.tsukuba.ac.jp

We grew $BaSi_2$ films on Ge(111) substrates by various growth methods based on molecular beam epitaxy (MBE). First, we attempted to form $BaSi_2$ films directly on Ge(111) by MBE without templates. We next formed $BaSi_2$ films using $BaGe_2$ templates as commonly used for MBE growth of $BaSi_2$ on Si substrates. Contrary to our prediction, the lateral growth of $BaSi_2$ was not promoted by these two methods; $BaSi_2$ formed not into a continuous film but into islands. Although streaky patterns of reflection high-energy electron diffraction were observed inside the growth chamber, no X-ray diffraction lines of $BaSi_2$ were observed in samples taken out from the growth chamber. Such $BaSi_2$ islands were easily to get oxidized. We finally attempted to form a continuous $BaSi_2$ template layer on Ge(111) by solid phase epitaxy, that is, the deposition of amorphous Ba-Si layers onto MBE-grown $BaSi_2$ epitaxial islands, followed by post annealing. We achieved the formation of an approximately 5-nm-thick $BaSi_2$ continuous layer by this method. Using this $BaSi_2$ layer as a template, we succeeded in forming *a*-axis-oriented 520-nm-thick $BaSi_2$ epitaxial films on Ge substrates, although (111)-oriented Si grains were included in the grown layer. We next formed a B-doped p-$BaSi_2$(20 nm)/n-Ge(111) heterojunction solar cell. A wide-spectrum response from 400 to 2000 nm was achieved. At an external bias voltage of 1 V, the external quantum efficiency reached as high as 60%, demonstrating the great potential of $BaSi_2$/Ge combination. However, the efficiency of a solar cell under AM1.5 illumination was quite low (0.1 %). The origin of such a low efficiency was examined.

1. Introduction

Photovoltaic solar cells have been studied worldwide as one of the new energy sources. The mainstream material for photovoltaics is crystalline silicon (c-Si). Panasonic Corp. achieved a record conversion efficiency η = 25.6% in a back-contact crystalline Si (c-Si) heterojunction with intrinsic thin-layer solar cells.[1)] However, η is reaching close to the performance limit. Thin-film solar cells, such as $CuInGaSe_2$,[2,3)] CdTe,[4,5)] and perovskite solar cells,[6,7)] have also attracted much attention in studies to realize higher-η solar cells with lower cost. However, these materials consist of critical raw materials. For photovoltaic solar cells to be more widely available in ordinary homes, it is preferable to replace these materials with semiconductors composed of earth-abundant and environment-friendly elements. Si thin-film solar cells have also been studied extensively,[8-13)] however, it is not easy to attain η higher than 20% because the absorption coefficient α of Si is relatively small. Among such materials, we have been doing research on orthorhombic $BaSi_2$. It has an indirect band gap E_g of 1.3 eV at room temperature (RT).[14)] Besides, α reaches 3.0×10^4 cm^{-1} at 1.5 eV, which is more than 30 times larger than that of c-Si.[15-17)] In addition, a minority-carrier diffusion length L of ca. 10 μm and a minority-carrier lifetime of ca. 10 μs of intrinsically n-$BaSi_2$ are sufficiently large for thin-film solar cell applications.[18-20)] Impurity doping of $BaSi_2$ enables the control of the carrier type and carrier concentration. For instance, we can control the hole concentration p in a wide range between 10^{16} and 10^{19} cm^{-3} by boron (B) doping.[21,22)] For these reasons, $BaSi_2$ could be a light absorber material for thin-film solar cells.[23)] $BaSi_2$ can be grown epitaxially on a Si(111) surface with a small lattice mismatch.[24-26)] We have recently examined the performance of p-$BaSi_2$/n-Si heterojunction solar cells[27)] and realized an η of approximately 10% and a short-circuit current density of 35.2 mA/cm^2.[28)] In these p-$BaSi_2$/n-Si solar cells, a large conduction-band offset E_C = 0.85 eV and a valence-band offset ΔE_V = 0.65 eV due to the low electron affinity of $BaSi_2$ (3.2 eV)[29)] promote the separation of photogenerated carriers in the layers. However, there are several problems in this structure that hinder the achievement of a much higher η. First, the band gap of $BaSi_2$ (1.3 eV) is closer to that of Si (1.1 eV), thus their light absorption wavelengths overlap to a large extent. Thus, the maximum short-circuit current density J_{SC} is limited. Second, the α of c-Si is small. Hence, it is difficult to decrease the total thickness of p-$BaSi_2$/n-Si layers when we utilize both $BaSi_2$ and Si as absorber materials. Third, cracks are easily generated in the $BaSi_2$ layer

owing to a large difference in thermal expansion coefficient between $BaSi_2$ and Si.[30,31] Replacing Si with Ge as a substrate is one of the solutions to these problems. Ge has the same diamond structure as Si, and its lattice constant is close to that of Si. We thus anticipate $BaSi_2$ films to be grown epitaxially on Ge(111). Besides, Ge is an excellent bottom cell material of a tandem-structure solar cell.[32,33] Therefore, $BaSi_2$ (E_g = 1.3 eV)/Ge (E_g =0.67 eV) heterojunction solar cells might absorb light with a wider wavelength range. Moreover, Ge has large α and L. We thus expect to achieve a larger J_{SC} in p-$BaSi_2$/n-Ge heterojunction solar cells. Furthermore, the thermal expansion coefficient of Ge is closer to that of $BaSi_2$ than that of Si; thus the crack formation in $BaSi_2$ might be suppressed.[34] In addition, (111)-oriented polycrystalline Ge can be formed on SiO_2 by Al-induced crystallization,[35] thereby enabling the growth of highly oriented $BaSi_2$ films even on inexpensive substrates. However, there have been no reports thus far about the formation of $BaSi_2$ films on Ge substrates.

In this work, we aim to achieve the epitaxial growth of $BaSi_2$ on Ge(111). First, we focused on the formation of continuous $BaSi_2$ films on Ge(111). We employed three kinds of growth methods for this purpose, that is, the growth of $BaSi_2$ (1) without any templates, (2) with $BaGe_2$ templates, and (3) with solid phase epitaxy (SPE) $BaSi_2$ templates. Finally, we formed B-doped p-$BaSi_2$(20 nm)/n-Ge heterojunction diodes using the optimum growth method and characterized their electrical and optical properties.

2. Experimental methods

In this study, we used an ion-pumped molecular beam epitaxy (MBE) systems (R-DEC) equipped with a standard Knudsen cell for Ba and an electron-beam evaporation source for Si. For the epitaxial growth of continuous $BaSi_2$ films on Ge(111), we fabricated samples A, B, and C, using different templates. The growth procedures for samples A-C are schematically shown in Fig. 1. For sample A, Ba and Si were codeposited on a heated p-Ge(111) substrate (resistivity $\rho <$ 0.01 Ω·cm) at the substrate temperature T_S = 580 °C to form 200-nm-thick $BaSi_2$ without any templates by MBE. For sample B, we employed the two-step growth technique, which is the conventional growth method for $BaSi_2$ on Si(111).[25,26] We firstly deposited Ba on a heated-Ge(111) substrate at T_S = 500 °C to form a 30 nm $BaGe_2$ template by reactive deposition epitaxy (RDE). $BaGe_2$ has the same orthorhombic crystal structure as $BaSi_2$, and its lattice constants are close to those of

$BaSi_2$.[15,17] We thus anticipated $BaGe_2$ to act as a template layer for $BaSi_2$ overlayers and grew 150-nm-thick $BaSi_2$ at 580 °C by MBE. For sample C, we utilized a $BaSi_2$ layer grown by SPE as a template for the subsequent $BaSi_2$ overlayers. First of all, we formed 2-nm-thick $BaSi_2$ by MBE. This $BaSi_2$ was used as nucleus for the subsequent SPE layer. Next, we codeposited 3-nm-thick Ba and Si amorphous layers at 200 °C at an atomic ratio of Si/Ba = 2, followed by post-annealing at 700 °C for 5 min. On this template, we fabricated 520-nm-thick $BaSi_2$ films at 580 °C by MBE.

As described later, we succeeded to form $BaSi_2$ continuous films by the third method used for sample C. Using this method, we next formed p-$BaSi_2$/n-Ge(111) solar cells, sample D. We grew a 20-nm-thick B-doped p-$BaSi_2$ layer on n-Ge(111) (ρ ~ 40 Ω·cm). The growth conditions of sample D were almost the same as those of sample C. During the MBE growth, Ba, Si, and B were codeposited on the SPE-$BaSi_2$ templates. We set the B concentration to 2×10^{18} cm^{-3}, at which the hole concentration p is close to B concentration, meaning that the activation ratio of B atoms is approximately 1.[27] After that, the $BaSi_2$ layer was capped *in situ* with a 3-nm-thick amorphous-Si (a-Si) layer at 180 °C.[36] In our previous studies, we found that the minority-carrier lifetime of $BaSi_2$ was reproducibly improved by depositing an a-Si capping layer.[37] Besides, the potential barrier height of a-Si for photogenerated holes in n-$BaSi_2$ was found to be –0.2 eV,[38] whereas that of native oxide was 3.9 eV.[39] Smooth extraction of photogenerated carriers through the a-Si capping layer was proved previously.[28] For the evaluation of optical properties, 1-mm-diameter and 70-nm-thick indium-tin-oxide (ITO) electrodes were sputtered on the front surface and Al electrodes were formed on the back surface of the n-Ge substrate. The crystalline quality of grown films was characterized by reflection high-energy electron diffraction (RHEED) and θ-2θ X-ray diffraction (XRD) with Cu Kα radiation. The composition of grown layers was analyzed by high-angle annular dark field scanning transmission electron microscopy (HAADF-STEM) and energy dispersive X-ray (EDX) spectrometry. The surface morphologies were observed by atomic force microscopy (AFM). We also conducted the current mapping of the sample by conductive AFM (c-AFM) in order to find the current leakage paths. Current density versus voltage (J-V) curves were measured under standard AM1.5, 100 mW/cm^2 illumination at 25 °C. Photoresponse and reflectance spectra were measured at RT by the lock-in technique using a xenon lamp with a 25-cm-focal-length single monochromator

(Bunko Keiki SM-1700A and RU-60N). Light intensity was calibrated using a pyroelectric sensor (Melles Griot 13PEM001/J). All measurements were performed using a mask with 1-mm-diameter holes.

3. Results and discussion

3.1 Growth of $BaSi_2$ epitaxial films on Ge(111)

We first discuss the results of sample A, that is, $BaSi_2$ grown directly on the Ge(111) substrate by MBE. Figure 2(a) shows the θ-2θ XRD pattern of sample A. Hereafter the peak labeled with an asterisk indicates diffraction from the substrate. The inset shows the RHEED pattern taken after the MBE growth. The RHEED pattern was observed along the Ge[$11\bar{2}$] azimuth. As can be seen in the RHEED pattern, a sharp streaky pattern was observed, which indicates that *a*-axis-oriented $BaSi_2$ was grown on the Ge(111) substrate. However, we did not observe any diffraction lines originating from $BaSi_2$ in the XRD pattern after exposing the sample to air. These observations were not made in $BaSi_2$ epitaxial films on Si(111). In order to determine the origin, we performed an AFM observation of sample A. A 5×5 μm^2 topographic image and the cross-sectional profile along the white line are shown in Fig. 2(b). The height of the grain is found to be approximately 260 nm from the cross-sectional profile. This height is much larger than the deposited thickness (200 nm) monitored using a quartz crystal microbalance, meaning that $BaSi_2$ formed not into a continuous film but into islands. We also found that the surface color changed gradually after exposing sample A to air. We thus speculate that oxygen and moisture in the air entered into the gaps between the $BaSi_2$ islands, and the entire $BaSi_2$ was oxidized.

Next, we examined sample B, $BaSi_2$/$BaGe_2$ template/Ge(111). Figure 3(a) shows the θ-2θ XRD pattern of sample B. A streaky RHEED pattern was observed after the MBE growth, indicating that *a*-axis-oriented $BaSi_2$ was also grown on the $BaGe_2$ template. However, again, we observed no diffraction lines of $BaSi_2$. As shown in the 5×5 μm^2 AFM image and the cross-sectional profile along the white line in Fig. 3(b), the height of $BaSi_2$ islands (300 nm) was larger than the predicted grown thickness, suggesting that $BaSi_2$ was not a continuous film. Hence, the entire $BaSi_2$ crystals were oxidized, leading to the disappearance of diffraction peaks of $BaSi_2$ in Fig. 3(a). The results of samples A and B indicate that the lateral growth of $BaSi_2$ is quite limited on Ge(111) and $BaGe_2$ surfaces,

thereby the surface area of $BaSi_2$ on Ge(111) is quite large. This is the reason why $BaSi_2$ is easily oxidized on a Ge(111) substrate than on a Si(111) substrate.

Here, we discuss the reason why $BaSi_2$ on Ge(111) formed into not a continuous film but into islands. The growth of thin films can be divided into three modes, the Frank-van der Merwe (FW) mode (layer-by-layer growth), the Stranski-Krastranov (SK) mode [three-dimensional (3D) clusters on the first monolayer], and the Volmer-Weber (VW) mode (island growth). These growth modes are determined by a surface or an interfacial energy for the lattice-matched systems. According to the growth of $InP_{1-x}Sb_x$ on InP substrates, the FM mode is dominant and $InP_{1-x}Sb_x$ becomes a continuous film when the InSb composition is small since the lattice mismatch between $InP_{1-x}Sb_x$ and the InP substrate is small. In contrast, the SK mode or the VM mode is dominant and 3D clusters of $InP_{1-x}Sb_x$ are likely to form when the InSb composition is large.[40] The epitaxial relationship between $BaSi_2$ and Si(111) is $BaSi_2(100)$ || Si(111) with $BaSi_2[001]$ || $Si[1\bar{1}0]$. $BaSi_2$ on Ge(111) shows the same epitaxial relationship. The lattice mismatches of $BaSi_2$ on Si(111) are small, that is, 0.1% along $Si[1\bar{1}0]$ and 1.1% along $Si[\bar{1}\,\bar{1}2]$; however, they are 3.4 and 1.7% for $BaSi_2$ on Ge(111), respectively. Hence, we speculate that the island growth of $BaSi_2$ arises from a large lattice mismatch between $BaSi_2$ and Ge(111).

In order to form continuous $BaSi_2$ films on a Ge(111) substrate, we focused on the formation of a continuous $BaSi_2$ template layer in sample C using the SPE template shown in Fig. 1. Figures 4(a) and 4(b) show the RHEED pattern after the MBE growth and the θ-2θ XRD pattern of sample C, respectively. We see the sharp streaky RHEED pattern of $BaSi_2$. In addition, intense (100)-oriented diffraction peaks can be observed in Fig. 4(b). Contrary to our prediction, however, we also observed the intense diffraction peak of Si(111). This means that (111)-oriented Si grains were included in the grown layers. Figure 4(c) shows a 5×5 μm^2 AFM image and the cross-sectional profile along the white line in sample C. The grain height is approximately 30 nm at most, which is much smaller than the total growth thickness of 520 nm. Therefore, we can state that we succeeded in growing a highly *a*-axis-oriented $BaSi_2$ epitaxial film using the SPE-$BaSi_2$ templates. As mentioned above, (111)-oriented Si grains were included in the grown layers. In order to confirm this, we performed HAADF-STEM and EDX measurements on the same area of sample C, as shown in Figs. 5(a) and 5(b), respectively. The presence of Si grains in the grown layer was proved. Since

these Si grains have the (111) orientation, as shown in Fig. 4(b), we speculate that these Si grains stem from the (111)-oriented Ge surface, and exist in the form of pillars. The origin of Si grains, namely, the excess Si in the grown layer, is the deviation from stoichiometry due to evaporation of Ba atoms from the sample surface during the post annealing for SPE. Now, we can surely form $BaSi_2$ epitaxial films on Ge(111), and the next step is to form p-$BaSi_2$/n-Si solar cells.

3.2 Evaluation of p-$BaSi_2$/n-Ge(111) heterojunction diodes

Before discussing the properties of sample D, p-$BaSi_2$ (20 nm, $p = 2 \times 10^{18}$ cm^{-3})/n-Ge ($n = 4 \times 10^{13}$ cm^{-3}), we describe the calculated band alignment in Fig. 6. The electron affinities of $BaSi_2$ ($q\chi^{BaSi_2}$) and Ge ($q\chi^{Ge}$) are 3.2 and 4.0 eV, respectively.[29] As shown in Fig. 6, $\Delta E_C = 0.8$ eV and $\Delta E_V = 0.17$ eV at the interface. The built-in potential V_D is given by

$$V_D = \frac{E_g^{BaSi_2} + q\chi^{BaSi_2} - k_B T \ln(\frac{N_V^{BaSi_2}}{p})}{q} - \frac{q\chi^{Ge} + k_B T \ln(\frac{N_C^{Ge}}{n})}{q}, \quad (1)$$

where q is the elemental charge, k_B is the Boltzmann constant, $N_V^{BaSi_2}$ is the effective density of states in the valence band of $BaSi_2$, N_C^{Ge} is that in the conduction band of Ge, p is the hole concentration of p-$BaSi_2$, and n is the electron concentration of the n-Ge. Assuming that $N_V^{BaSi_2} = 2.0 \times 10^{19}$ cm^{-3},[41] and $N_C^{Ge} = 1.1 \times 10^{19}$ cm^{-3}, V_D is calculated to be 0.11 V. Note that the separation of photogenerated electrons and holes is assisted by the band offsets, although V_D is small.

Figure 7 shows the external quantum efficiency (*EQE*) spectra of sample D at different bias voltages applied to the p-$BaSi_2$ with respect to n-Ge. We also show the *EQE* spectra of a p-$BaSi_2$/n-Si heterojunction solar cell for comparison.[27] We found that the spectral response extends in a longer-wavelength range in sample D. This means that the p-$BaSi_2$/n-Ge heterojunction diode can absorb lights in a wider wavelength range. However, the *EQE* of sample D ($V = 0$ V) is much smaller than that of p-$BaSi_2$/n-Si.

Figure 8(a) presents the first quadrant of the *J*-*V* curve under the illumination. We

achieved solar cell operation. However, J_{SC} and the open-circuit voltage V_{OC} were quite small. Figure 8(b) shows the *J*-*V* curve in the dark and that under AM1.5 illumination with bias voltages between −1.0 and 1.0 V. The blue broken line shows the photocurrent density J_{ph}, that is, the difference between *J* in the dark and that under illumination. We obtained large J_{ph} values under negative bias voltages. This result indicates that p-$BaSi_2$/n-Ge has great potential for thin-film solar cell applications. However, the problem is that the reverse current did not saturate. To accurately obtain the shunt resistance R_{SH} in the diode, we adopted a technique described in Ref. 42. Using the photodiode equation, R_{SH} can be given as

$$\frac{dV}{dJ} = SR_S + \frac{\gamma k_B T}{q}\left[\frac{1-(SR_{SH})^{-1}\,dV/dJ}{J + J_{SC} - (SR_{SH})^{-1}V}\right]. \quad (1)$$

Here, *S* is the device area, R_S is the series resistance, γ is the diode ideality factor, k_B is the Boltzmann constant, *T* is the absolute temperature, *q* is the elemental charge, and J_{SC} is the short-circuit current density. Parameters are summarized in Table 1. The reverse-bias saturation current density J_0 was 5.43×10^{-2} mA/cm^2. This value is 2–3 orders of magnitude higher than that for p-$BaSi_2$/n-Si heterojunction diodes,[28,36] suggesting the carrier recombination via defects. R_{SH} was 1.57 kΩ, which is more than one order of magnitude smaller than those obtained for p-$BaSi_2$/n-Si heterojunction diodes.[28,36] Small R_{SH} indicates the presence of current leakage paths through the pn junction.

In order to investigate such leakage paths, we observed the sample surface by AFM and c-AFM, and Figs. 9(a) and 9(b) show their respective images of the same area. The c-AFM image was taken under a bias voltage of 1.5 V across the top and bottom electrodes. We see some protuberances on the sample surface in Fig. 9(a). In addition, the current does not uniformly flow across the junction in Fig. 9(b). There seems to be current leakage paths in and around some protuberances. This is why the reverse current density did not saturate in Fig. 8(b). Although there is no evidence showing that the protuberances in Fig. 9(a) are Si grains, we speculate that the Si grains act as current leakage paths. This is because the R_{SH}

of p-$BaSi_2$/n-Ge solar cells was much smaller than that of p-$BaSi_2$/n-Si solar cells, and the main difference between the two diodes is the presence of Si grains in the p-$BaSi_2$ layers. It can safely be stated that we need to suppress the formation of protuberances observed in Fig. 9(a) in order to improve the properties of p-$BaSi_2$/n-Ge heterojunction diodes.

4. Conclusions

We attempted to form *a*-axis-oriented $BaSi_2$ epitaxial layers on Ge(111) substrates using three kinds of growth methods. We firstly tried to grow $BaSi_2$ on Ge(111) at 580 °C by MBE without any templates. We next attempted to form $BaSi_2$ at the same temperature using RDE-grown $BaGe_2$ templates. $BaSi_2$ was surely grown on the Ge substrates by these two methods, as shown by the streaky RHEED patterns, inside the growth chamber. It was proved by AFM that $BaSi_2$ formed not into a continuous film but into islands and that these $BaSi_2$ islands were easily oxidized in air. Highly (100)-oriented $BaSi_2$ continuous films were formed by MBE at 580 °C using the $BaSi_2$ continuous template grown by SPE. (111)-oriented Si was included in the grown layer. With this growth method, we fabricated B-doped p-$BaSi_2$(20 nm)/n-Ge heterojunction diodes. We attained an extremely large J_{ph} at negative bias voltages owing to a wide-spectrum response. The solar cell operation was achieved in p-$BaSi_2$/n-Ge; however, J_{SC} and V_{OC} were quite limited partly because of the small R_{SH} (1.57 kΩ). To overcome this problem, we need to suppress the current leakage through the pn junctions.

Acknowledgments

The authors thank Dr. N. Yoshizawa and Mr. N. Saito of the National Institute of Advanced Industrial Science and Technology for their HAADF-STEM and EDX observations. This work was financially supported by the Japan Science and Technology Agency (JST/CREST) and by a Grant-in-Aid for Scientific Research A (15H02237) from the Japan Society for the Promotion of Science (JSPS). R.T. was financially supported by a Grant-in-Aid for JSPS Fellows (15J02139).

References

1) K. Masuko, M. Shigematsu, T. Hashiguchi, D. Fujishima, M. Kai, N. Yoshimura, T. Yamaguchi, Y. Ichihashi, T. Mishima, N. Matsubara, T. Yamanishi, T. Takahama, M. Taguchi, E. Maruyama, and S. Okamoto, IEEE J. Photovoltaics **4**, 1433 (2014).
2) P. Jackson, D. Hariskos, R. Wuerz, O. Kiowski, A. Bauer, T. M. Friedlmeier, and M. Powalla, Phys. Status Solidi: Rapid Res. Lett. **9**, 28 (2015).
3) S. Merdes, F. Ziem, T. Lavrenko, T. Walter, I. Lauermann, M. Klingsporn, S. Schmidt, F. Hergert, and R. Schlatmann, Prog. Photovoltaics **23**, 1493 (2015).
4) H. A. Mohamed, Thin Solid Films **589**, 72 (2015).
5) W. W. Yu, L. Qu, W. Guo, and X. Peng, Chem. Mater. **15**, 2854 (2003).
6) J. Burschka, N. Pellet, S. J. Jin Moon, R. Humphry-Baker, P. Gao, M. K. Nazeeruddin, and Michael Grätzel, Nature **499**, 316 (2013).
7) M. Liu, M. B. Johnston, and H. J. Snaith, Nature **501**, 395 (2013).
8) J. Müller, B. Rech, J. Springer, and M. Vanecek, Sol. Energy **77**, 917 (2004).
9) Michael Berginski, J. Hüpkes, M. Schulte, G. Schöpe, H. Stiebig, and Bernd Rech, J. Appl. Phys. **101**, 074903 (2007).
10) H. Sai, Y. Kanamori, and M. Kondo, Appl. Phys. Lett. **98**, 113502 (2011).
11) S. Kim, J. Chung, H. Lee, J. Park, Y. Heo, and H. Lee, Sol. Energy Mater. Sol. Cells **119**, 26 (2013).
12) T. Matsui, H, Sai, K. Saito, and M. Kondo, Prog. Photovoltaics **21**, 1363 (2013).
13) C. Trompoukis, I. Abdo, R. Cariou, I. Cosme, W. Chen, O. Deparis, A. Dmitriev, E, Drouard, M. Foldyna, E. G. Caurel, I. Gordon, B. Heidari, A. Herman, L. Lalouat, K. Lee, J. Liu, K. Lodewijks, F. Mandorlo, I. Massiot, A. Mayer, V. Mijkovic, J. Muller, R. Orobtchouk, G. Poulain, P. Prod'Homme, P. R. i Cabarrocas, C. Seassal, J. Poortmans, R. Mertens, O. E. Daif, and V. Depauw, Phys. Status Solidi A **212**, 140 (2015).
14) K. Morita, Y. Inomata, and T. Suemasu, Thin Solid Films **508**, 363 (2006).
15) D. B. Migas, V. L. Shaposhnikov, and V. E. Borisenko, Phys. Status Solidi B **244**, 2611 (2007).
16) K. Toh, T. Saito, and T. Suemasu, Jpn. J. Appl. Phys. **50**, 068001 (2011).
17) M. Kumar, N. Umezawa, and M. Imai, J. Appl. Phys. **115**, 203718 (2014).
18) M. Baba, K. Toh, K. Toko, N. Saito, N. Yoshizawa, K. Jiptner, T. Sakiguchi, K. O. Hara,

N. Usami, and T. Suemasu, J. Cryst. Growth **348**, 75 (2012).

19) K. O. Hara, N. Usami, K. Toh, M. Baba, K. Toko, and T. Suemasu, J. Appl. Phys. **112**, 083108 (2012).
20) K. O. Hara, N. Usami, K. Nakamura, R. Takabe, M. Baba, K. Toko, and T. Suemasu, Appl. Phys. Express **6,** 112302 (2013).
21) M. Ajmal Khan, K. O. Hara, W. Du, M. Baba, K. Nakamura, M. Suzuno, K. Toko, N. Usami, and T. Suemasu, Appl. Phys. Lett. **102**, 112107 (2013).
22) M. Ajmal Khan, K. Nakamura, W. Du, K. Toko, N. Usami, and T. Suemasu, Appl. Phys. Lett. **104**, 252104 (2014).
23) T. Suemasu, Jpn. J. Appl. Phys. **54**, 07JA01 (2015).
24) Y. Inomata, T. Nakamura, T. Suemasu, and F. Hasegawa, Jpn. J. Appl. Phys. **43**, 4155 (2004).
25) Y. Inomata, T. Nakamura, T. Suemasu, and F. Hasegawa, Jpn. J. Appl. Phys. **43**, L478 (2004).
26) R. Takabe, K. Nakamura, M. Baba, W. Du, M. A. Khan, K. Toko, M. Sasase, K. O. Hara, N. Usami, and T. Suemasu, Jpn. J. Appl. Phys. **53**, 04ER04 (2014).
27) D. Tsukahara, S. Yachi, H. Takeuchi, R. Takabe, W. Du, M. Baba, Y. Li, K. Toko, N. Usami, and T. Suemasu, Appl. Phys. Lett. **108**, 152101 (2016).
28) S. Yachi, R. Takabe, H. Takeuchi, K. Toko, and T. Suemasu, Appl. Phys. Lett. **109**, 072103 (2016).
29) T. Suemasu, K. Morita, M. Kobayashi, M. Saida, and M. Sasaki, Jpn. J. Appl. Phys. **45**, L519 (2006).
30) M. Okaji, Int. J. Thermophys. **9**, 1101 (1988).
31) M. Imai, Jpn. J. Appl. Phys. **50**, 101801 (2011).
32) T. Takamoto, M. Kaneiwa, M. Imaizumi, M. Yamaguchi, Prog. Photovoltaics **13**, 495 (2005).
33) M. A. Green, M. J. Keevers, I. Thomas, J. B. Lasich, K. Emery, and R. R. King, Prog. Photovoltaics **23**, 685 (2015).
34) D. F. Gibbons, Phys. Rev. **22**, 136 (1958).
35) K. Toko, M. Kurosawa, N. Saitoh, N. Yoshizawa, N. Usami, M. Miyao, and T. Suemasu, Appl. Phys. Lett. **101**, 072106 (2012).

36) R. Takabe, S. Yachi, W. Du, D. Tsukuhara, H. Takeuchi, K. Toko, and T. Suemasu, AIP Adv. **6**, 085107 (2016).
37) R. Takabe, K. O. Hara, M. Baba, W. Du, N. Shimada, K. Toko, N. Usami, and T. Suemasu, J. Appl. Phys. **115**, 193510 (2014).
38) R. Takabe, H. Takeuchi, W. Du, K. Ito, K. Toko, S. Ueda, A. Kimura, and Takashi Suemasu, J. Appl. Phys. **119**, 165304 (2016).
39) R. Takabe, W. Du, K. Ito, H. Takeuchi, K. Toko, S. Ueda, A. Kimura, and T. Suemasu, J. Appl. Phys. **119**, 025306 (2016).
40) K. Nakajima, Jpn. J. Appl. Phys. **38**, 1875 (1999).
41) D. Tsukahara, M. Baba, S. Honda, Y. Imai, K. O. Hara, N. Usami, K. Toko, J. W. Werner, and T. Suemasu, J. Appl. Phys. **116**, 123709 (2014).
42) J. R. Sites and P. H. Mauk, Sol. Cells **27**, 411 (1989).

Table I. Solar cell properties of specifically for sample D.

J_{SC} (mA/cm^2)	V_{OC} (V)	η (%)	R_S (Ω)	R_{SH} (kΩ)	γ	J_0 (mA/cm^2)
6.46	0.013	0.1	139	1.57	3.83	5.43×10^{-2}

Figure Captions

Fig. 1. Schematics of growth procedures for samples A-C.

Fig. 2. (a) θ-2θ XRD pattern of sample A, $BaSi_2$/Ge(111). The inset shows the RHEED pattern taken after the MBE growth along the Ge[$11\bar{2}$] azimuth. (b) 5 × 5 μm^2 AFM topographic image and cross-sectional profile along the white line in sample A.

Fig. 3. (a) θ-2θ XRD pattern of sample B, $BaSi_2$/$BaGe_2$/Ge(111). The inset shows the RHEED pattern of sample B after MBE growth. (b) 5 × 5 μm^2 AFM image and cross-sectional profile along the white line in sample B.

Fig. 4. (a) RHEED pattern after MBE growth along the Ge[$11\bar{2}$] azimuth, (b) θ-2θ XRD pattern, and (c) 5 × 5 μm^2 AFM image and cross-sectional profile along the white line in sample C.

Fig. 5. (Color online) (a) HAADF-STEM and (b) EDX images of the same area in sample C.

Fig. 6. Calculated band alignment of p-$BaSi_2$ (20 nm, $p = 2 \times 10^{18}$ cm^{-3})/n-Ge ($n = 4 \times 10^{13}$ cm^{-3}) heterojunction.

Fig. 7. (Color online) *EQE* spectra of sample D, B-doped p-$BaSi_2$/n-Ge, at various bias voltages applied to p-$BaSi_2$ with respect to n-Ge. The blue line shows the *EQE* of p-$BaSi_2$/n-Si heterojunction solar cell.[27)]

Fig. 8. (Color online) (a) First quadrant of the *J*-*V* curve of sample D, B-doped p-$BaSi_2$/n-Ge. (b) *J*-*V* characteristics in the dark and under AM 1.5 illumination with the voltage range between −1 and 1 V. The blue broken line shows the photocurrent density.

Fig. 9. (Color online) (a) AFM topographic image and (b) c-AFM images of the same area in sample D, B-doped p-$BaSi_2$/n-Ge. c-AFM measurements were performed at the bias

voltage of 1.5 V across the top and bottom electrodes.

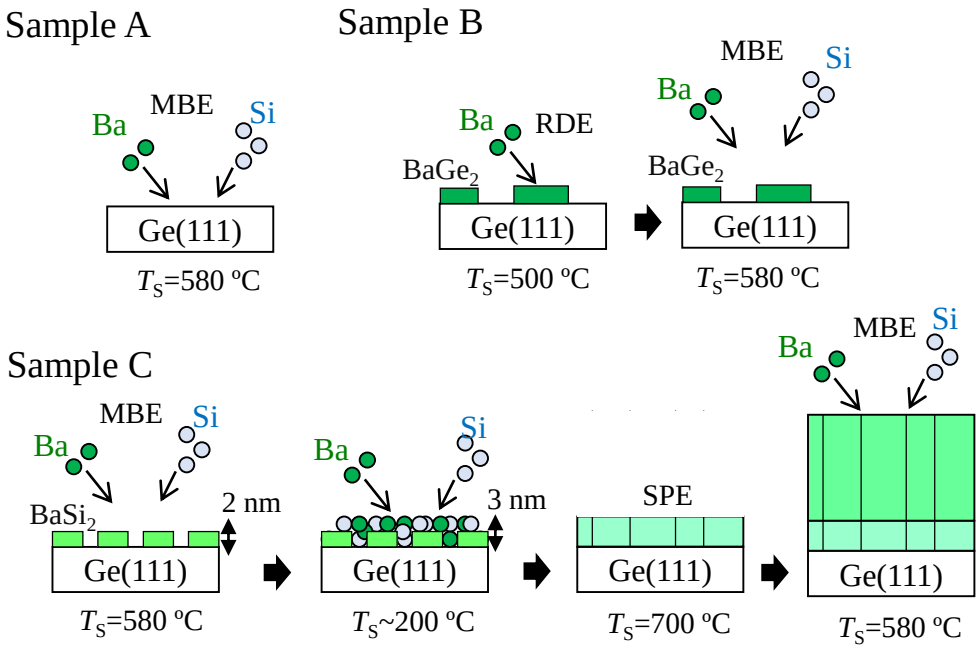
Sample A
Ba
MBE
Si
Ge(111)
T_S=580 ºC
Sample B
Ba
RDE
$BaGe_2$
Ge(111)
T_S=500 ºC
MBE
Si
Ba
$BaGe_2$
Ge(111)
T_S=580 ºC
Sample C
Ba
MBE
Si
$BaSi_2$
2 nm
Ge(111)
T_S=580 ºC
Ba
Si
3 nm
Ge(111)
T_S~200 ºC
SPE
Ge(111)
T_S=700 ºC
Ba
MBE
Si
Ge(111)
T_S=580 ºC

Fig. 1

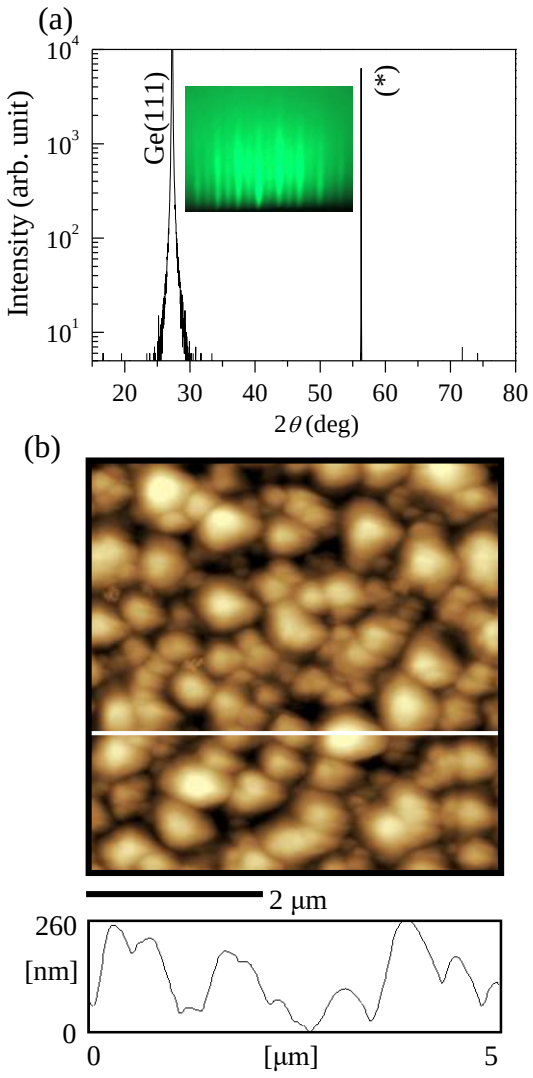

Fig. 2

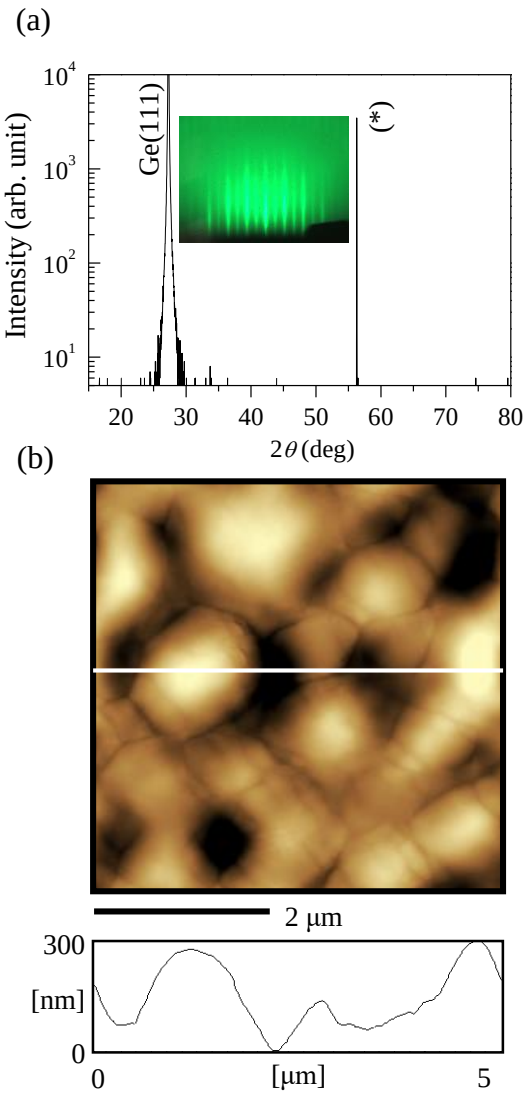

Fig. 3

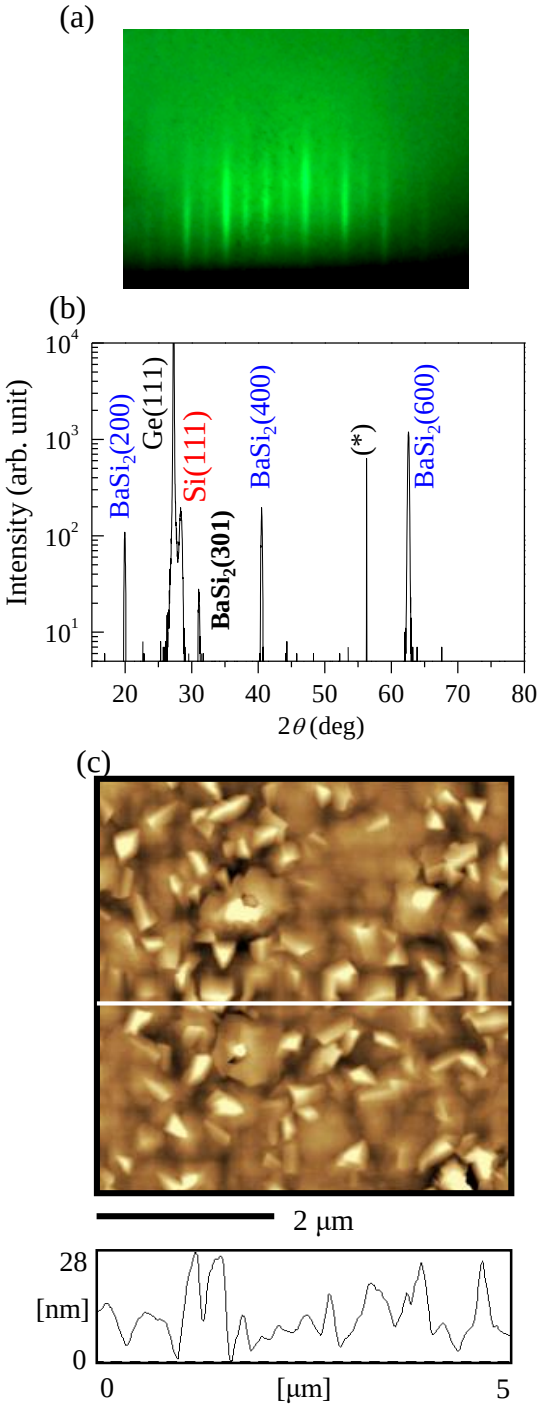
(a)
(b)
Intensity (arb. unit)
10^4
10^3
10^2
10^1
BaSi$_2$(200)
Ge(111)
Si(111)
BaSi$_2$(301)
BaSi$_2$(400)
(*)
BaSi$_2$(600)
20
30
40
50
60
70
80
2θ (deg)
(c)
2 μm
28
[nm]
0
0
[μm]
5

Fig. 4

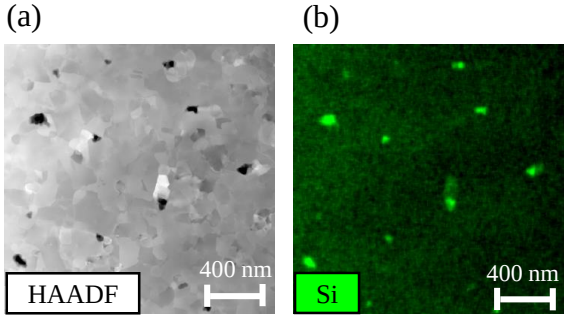

Fig. 5

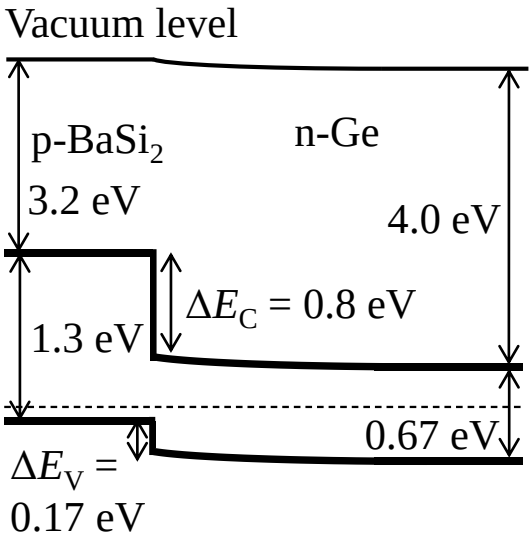
Vacuum level
p-BaSi2
3.2 eV
n-Ge
4.0 eV
ΔEC = 0.8 eV
1.3 eV
0.67 eV
ΔEV =
0.17 eV

Fig. 6

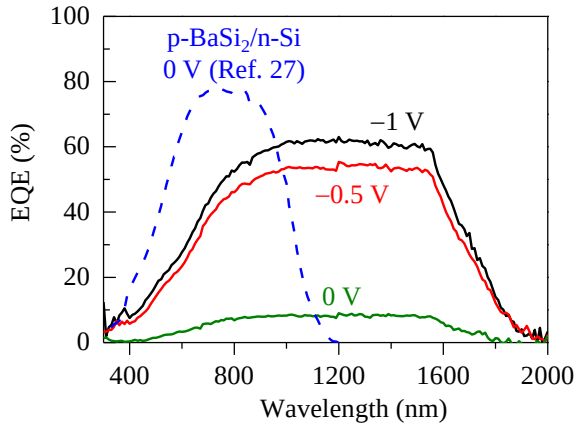
p-BaSi2/n-Si
0 V (Ref. 27)
−1 V
−0.5 V
0 V
EQE (%)
Wavelength (nm)
100
80
60
40
20
0
400
800
1200
1600
2000

Fig. 7

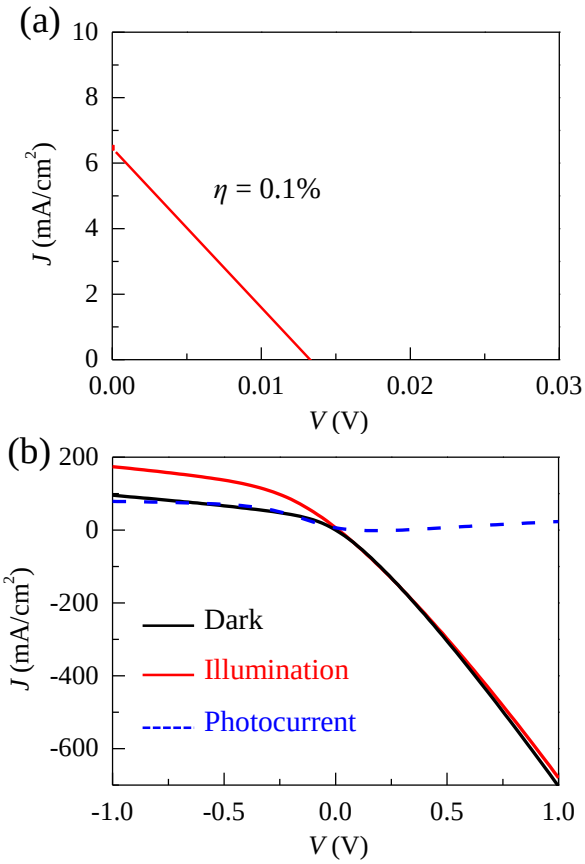
(a)
10
8
6
4
2
0
J (mA/cm2)
η = 0.1%
0.00
0.01
0.02
0.03
V (V)
(b)
200
0
-200
-400
-600
J (mA/cm2)
Dark
Illumination
Photocurrent
-1.0
-0.5
0.0
0.5
1.0
V (V)

Fig. 8

(a)

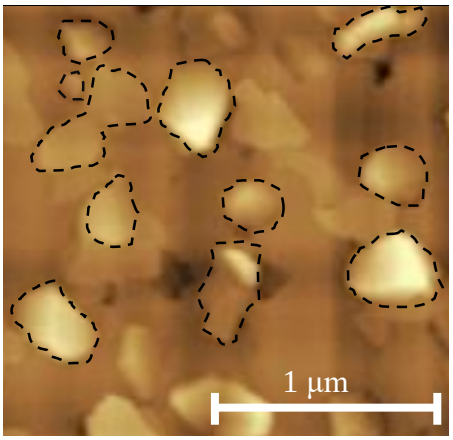

(b)

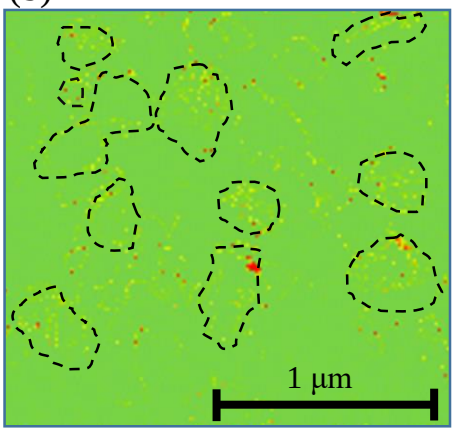

Fig. 9[24]